THE ASTROPHYSICAL JOURNAL, 520:548–563, 1999 August 1

EMISSION-LINE GALAXIES FROM THE NICMOS/*HUBBLE SPACE TELESCOPE* GRISM PARALLEL SURVEY

PATRICK J. MCCARTHY,[1] LIN YAN,[1] WOLFRAM FREUDLING,[2] HARRY I. TEPLITZ,[3,4] ELIOT M. MALUMUTH,[3,5] RAY J. WEYMANN,[1] MATTHEW A. MALKAN,[6] ROBERT A. E. FOSBURY,[2] JONATHAN P. GARDNER,[3,4] LISA J. STORRIE-LOMBARDI,[1] RODGER I. THOMPSON,[7] ROBERT E. WILLIAMS,[8] AND SARA R. HEAP[3]

Received 1998 December 10; accepted 1999 March 11

ABSTRACT

We present the first results of a survey of random fields with the slitless G141 ($\lambda_c = 1.5$ μm, $\Delta\lambda = 0.8$ μm) grism on the near-IR camera and multiobject spectrometer (NICMOS) on board the *Hubble Space Telescope* (*HST*). Approximately 64 arcmin^2 have been observed at intermediate and high Galactic latitudes. The 3 σ limiting line and continuum fluxes in each field vary from 7.5×10^{-17} to 1×10^{-17} ergs cm^{-2} s^{-1}, and from $H = 20$ to 22, respectively. Our median and area-weighted 3 σ limiting line fluxes within a 4 pixel aperture are nearly identical at 4.1×10^{-17} ergs cm^{-2} s^{-1} and are 60% deeper than the deepest narrowband imaging surveys from the ground. We have identified 33 emission-line objects and derive their observed wavelengths, fluxes, and equivalent widths. We argue that the most likely line identification is Hα and that the redshift range probed is from 0.75 to 1.9. The 2 σ rest-frame equivalent width limits range from 9 to 130 Å, with an average of 40 Å. The survey probes an effective comoving volume of 10^5 h_{50}^{-3} Mpc^3 for $q_0 = 0.5$. Our derived comoving number density of emission-line galaxies in the range $0.7 < z < 1.9$ is 3.3×10^{-4} h_{50}^3 Mpc^{-3}, very similar to that of the bright Lyman break objects at $z \sim 3$. The objects with detected emission lines have a median F160W magnitude of 20.4 (Vega scale) and a median Hα luminosity of 2.7×10^{42} ergs s^{-1}. The implied star formation rates range from 1 to 324 $M_\odot$ yr^{-1}, with an average [N II] $\lambda\lambda$6583, 6548 corrected rate of 21 $M_\odot$ yr^{-1} for $H_0 = 50$ km s^{-1} Mpc and $q_0 = 0.5$ (34 $M_\odot$ yr^{-1} for $q_0 = 0.1$).

Subject headings: galaxies: distances and redshifts — galaxies: Seyfert — galaxies: statistics — infrared: galaxies — surveys

1. INTRODUCTION

Spectroscopic surveys of galaxies at $z < 1$ have reached a reasonable level of maturity in recent years (e.g., Canada-France Redshift Survey, Lilly et al. 1996, Le Fevre et al. 1996; Canadian Network for Observational Cosmology, Yee, Ellingson, & Carlberg 1996). The use of specialized selection techniques has led to similar or greater gains at redshifts of approximately 3 and larger (Steidel et al. 1996; Dickinson 1999; Hu, Cowie, & McMahon 1998), with a few examples being identified to $z \sim 5$ (Dey et al. 1998; Weymann et al. 1998; Spinrad et al. 1998). However, in order to build a coherent picture of galaxy formation and evolution, we are hindered by two problems. The first is that we know little of properties of normal galaxies in the region $1 < z < 2$. Second, most high-redshift galaxies now known are selected at rest-frame UV wavelengths, where the degree of extinction is uncertain (e.g., Heckman et al. 1998). The detection of heavily dust-reddened galaxies at $z \sim 2$–3 in the submillimeter wavelength (Smail et al. 1997) suggests that high-redshift galaxies selected by UV colors represent only part of the population at these early epochs. At present, the estimates of the global star formation rates are uncertain, as they are based primarily on UV-selected samples (Pettini et al. 1997; Meurer et al. 1997).

One approach to dealing with both the scarcity of spectral signatures in the visible bandpass and the uncertainties arising from extinction is to observe in the near-IR. Until recently, the available detectors and spectrometers have made spectroscopic surveys in the near-IR impractical, and so most programs have been based on narrowband imaging ($\Delta\lambda \sim 1\%$) to search for strong emission-line objects, primarily in the K window where Hα can be detected for $1.9 < z < 2.6$. Two narrowband near-IR imaging surveys, covering several hundred square arcminutes, were carried out with the Calar Alto 3.5 m telescope (Thompson, Mannucci, & Beckwith 1996; Beckwith et al. 1998; Mannucci et al. 1998). The first Calar Alto survey targeted fields containing known quasars or radio galaxies, and the second the redshifts of damped Lyα or metal line absorption systems. The first survey discovered one emission-line galaxy at $z = 2.43$ over an area of 276 arcmin^2 to a 3 σ flux limit of 3.4×10^{-16} ergs cm^{-2} s^{-1}, while the second survey found 18 emission-line galaxies (16 objects with detected Hα and two with [O II] λ3727) over an area of 163 arcmin^2 to a 3 σ flux limit of 2×10^{-16} ergs cm^{-2} s^{-1}. To date the deepest narrowband near-IR imaging survey is that carried out by Teplitz, Malkan, & McLean (1999a) with NIRC on the Keck 10 m telescope. They found 13 emission-line galaxies in an 11 arcmin^2 area to a 3 σ flux limit of 7×10^{-17} ergs cm^{-2} s^{-1}. The target fields of this survey were also selected by matching the redshifts of quasar emission and metal absorption lines to their narrowband filters. The space densities of strong Hα emitting galaxies inferred from these surveys span more than 2 orders of magnitude. The large disparities in depths between the Calar Alto and Keck surveys and the strong biases introduced by selecting red-

[1] Observatories of the Carnegie Institution of Washington, 813 Santa Barbara Street, Pasadena, CA 91101.
[2] Space Telescope European Coordinating Facility, Karl-Schwarzschild-Strasse 2, D-85748 Garching bei München, Germany.
[3] NASA Goddard Space Flight Center, Code 681, Greenbelt, MD 20771.
[4] NOAO Research Associate.
[5] Raytheon STX Corporation, Lanham, MD 20706.
[6] Astronomy Department, University of California, Los Angeles, CA 90024-1562.
[7] Steward Observatory, University of Arizona, Tucson, AZ 85720.
[8] Space Telescope Science Institute, 3700 San Martin Drive, Baltimore, MD 21218.

shifts matched to known absorption-line clouds make comparisons between the surveys and with other measures of the average star formation rate nontrivial.

The near-IR camera and multiobject spectrometer (NICMOS) offered a unique opportunity to address this problem with multiobject spectroscopy. The wide field camera on NICMOS (Thompson et al. 1998) is equipped with three grisms that allow slitless spectroscopy over 0.75 arcmin^2 per exposure. The extremely low background at wavelengths below 1.9 μm allows for a sensitive low-resolution spectroscopic survey for Hα and other emission lines through volumes that are an order of magnitude larger than those available to narrowband imaging surveys due to the large redshift range sampled by the grism.

Throughout this paper, $H_0 = 50$ km s^{-1} Mpc^{-1} and $q_0 = 0.5$ are adopted unless explicitly indicated otherwise.

2. OBSERVATIONS

All of the data presented here were obtained with camera 3 on NICMOS using the G141 grism and the F160W and F110W broadband filters. The G141 spectral element covers the wavelength range from 1.1 to 1.9 μm with a mean dispersion of 8.1×10^{-3} μm pixel^{-1}. The nominal resolving power of the grism is 200. The actual resolution that is achieved is a function of the apparent image size and the camera 3 point-spread function (PSF). With the PSF present in the parallel observations, the realized resolution is rarely better than $R \sim 150$. Small variations in the PSF due to changes in the optical telescope assembly (e.g., breathing) and longer term changes in the internal structure of NICMOS introduce small variations in the maximum achievable resolution. As discussed in detail below, many of the objects detected in our survey are spatially resolved and the resolution of their G141 spectra is determined by the image size.

2.1. *Parallel Observing Mode and Scheduling*

All of the observations for this investigation were obtained with the *Hubble Space Telescope* (*HST*) operating in the parallel mode. While this allowed us to collect far more data than would be possible in a single primary program, it limited our ability to plan and execute the observations in a manner that optimized the science return. Useful data for this program first became available in 1997 October when the default position of the pupil alignment mirror was moved from the camera 2 optimized position to the best reachable position for camera 3. After that time, camera 3 parallels were scheduled during much of the time for which WFPC2 or STIS were the primary instruments. Most of the data in this investigation were obtained as part of a public service parallel program that was implemented and managed by the Space Telescope Science Institute. The observing algorithm was quite simple. In each full orbit, one of the following exposure sequences was selected: F160W and F110W imaging with exposure times of either 512 or 382 s, F160W (2×256 s) and G141 (2×896 s), or F110W (2×191 s) and G096 (2×896 s). The selection of the exposure sequence for any given orbit was nearly random but was weighted in favor of the purely imaging sequence for much of the 1997 October–1998 March period. After that time the balance was shifted toward spectroscopy with the grisms. All of these observations were planned and implemented by the STScI staff, with the guidance of John MacKenty.

The array was read using the STEP64 read pattern. A 2″ dither step was executed between each pair of direct or grism exposures. This dither step was made in the detector reference frame and was along array rows. The dither step and orientation were fixed, resulting in only two independent positions regardless of the number of exposures for any given target. Small moves executed as part of the primary observing plan introduced additional offsets for some of the longer pointings.

Approximately 10% of our data were obtained as part of a crafted guest observer parallel program that was implemented for a portion of the 1998 February–1998 May period. The basic approach was similar to the public parallel program, except that the dithering strategy was more complex. For each pointing we began with a number of F160W images with exposure times selected to equal 15% of the expected total duration of that particular pointing. Dither moves were executed between each exposure, but with step sizes and orientations that were nonredundant. The remainder of the orbit and subsequent orbits were devoted to G141 exposures with a dither pattern matched to that of the direct images. For a given exposure time the noise levels in these crafted observations were $\sim$20%–30% lower than those in the public parallels.

2.2. *Data Processing and Analysis*

2.2.1. *Two-dimensional Spectra*

We began our treatment of the data using the calibrated output from the STScI data processing pipeline. The pipeline reduction consists of dark current removal on a read-by-read basis, linearization, bad pixel masking, and cosmic-ray rejection. At this stage the data remain in the format of two-dimensional, single-frame images for each exposure. The principal elements of the reduction process that are accomplished by the pipeline to this point are the first order bias and dark subtraction, linearization, and cosmic-ray rejection. Our subsequent processing improves on the bias and dark subtraction, bad pixel masking, and more complete rejection of particle events. The calibrated grism exposures have not been corrected for the flat-field response and have not had the sky background removed. The flat-field response is a function of wavelength for each pixel, and so depends on the location of each object, and will not be the same for the object and the sky. The flat-field correction is applied during the one-dimensional spectral extraction.

We constructed a median sky frame for the G141 grism by combining the calibrated exposures for approximately 200 frames, covering 80 independent positions on the sky. We rejected observations made at low Galactic latitudes, as well as those centered on bright objects or crowded fields. This produced a high signal-to-noise uncorrected sky frame for use in the sky subtraction for each exposure. The observed background rates vary significantly from frame-to-frame depending on the ecliptic latitude and longitude. We subtracted a scaled version of the median sky from each calibrated two-dimensional spectral frame. The optimal scaling for the sky was found by minimizing the rms noise in two object-free regions of each frame. Very low spatial frequency structure remained in the background of many frames, primarily due to the shading effect in the NICMOS arrays. We removed a low-order surface from each frame. This surface was derived from a second-order polynomial fit

to an intermediate image constructed from the median of each column. This surface fitting was carried out separately in each quadrant of the detector, allowing us to remove small quadrant-to-quadrant bias variations. The individual sky-subtracted and shading-corrected frames were then shifted into registration, using offsets derived from the accompanying direct images. The registered two-dimensional spectra were then averaged with a bad pixel mask and 3 σ clipping applied to remove hot pixels and residual cosmic rays.

The direct images that are used to calibrate the extracted one-dimensional spectra were processed and combined using the same techniques as above, but without the sky subtraction and low-order surface-fitting correction steps.

2.2.2. *One-dimensional Spectral Extraction and Calibration*

The extraction and calibration of the one-dimensional spectra was carried out with the NICMOS-Look software developed at Space Telescope–European Coordinating Agency (Freudling et al. 1998). The extraction was done in the following way. First, the position and size of the objects previously identified as spectral line objects were interactively marked on the image display. The extraction region of the spectrum was then computed using transformations derived as part of the calibration program. The extracted spectra were corrected for the wavelength-dependent flat-field response on a pixel-by-pixel basis. For each pixel, the quantum efficiency for the extracted wavelength was estimated by interpolation from a series of narrowband flat-field exposures. Fluxes were calibrated by applying throughput curves previously derived from the observation of flux calibrators. The final one-dimensional spectra were obtained by adding the flux of all pixels that correspond to each wavelength bin. For some objects close to one of the edges of the grism images, only partial spectra could be extracted. Since there is a significant displacement between the location of objects on the direct images and their dispersed spectrum on the grism image, spectra for a few objects that fall outside the area covered by the direct images were extracted. In that case, the wavelength scale was estimated from the cutoff of the throughput curves at high and low wavelengths, which can easily be identified. For such objects, the wavelength scale is uncertain by about 0.01 μm.

The rms accuracy of the wavelength calibration for G141 is about 2×10^{-3} μm. Repeated calibration exposures have shown no changes larger than 3% in the wavelength zero point, or 1.5% in the dispersion. The flux calibration is based on observations of both white dwarfs and solar analogs during the NICMOS camera 3 campaigns. The accuracy of the spectrophotometry is limited by variations in the quantum efficiency within individual pixels. We estimate that the flux scale for an individual spectrum is accurate to about 10%.

Spectra were also extracted in a parallel effort by members of the team at the NASA Goddard Space Flight Center (GSFC) using software independent of the NICMOS-Look routines. The GSFC software followed a similar strategy to NICMOS-Look. Spectral positions on the chip were determined by the known offsets from the object location in the direct image. Extractions were performed on individual (unregistered) frames first, with registration left to the end. Each spectrum was extracted in a weighted box, similar to the procedure for the NICMOS-Look point-source extraction. The wavelength solution was confirmed by independent analysis of the same calibration data. Flat-fielding was performed using the same data cube of narrowband observations, interpolated to the wavelengths of the extracted pixels, and the flux calibration was performed based on independent analysis of the white dwarf observations. Finally, spectra were combined in wavelength space. Emission-line wavelengths derived from spectra extracted with the GSFC software were found to agree with the NICMOS-Look results to within 1 pixel (0.008 μm). Line fluxes and equivalent widths were measured using Gaussian fits to the line and polynomial fitting of the underlying continuum. The overall results of the extraction and analysis using the GSFC and ECF/NICMOS-Look software were similar.

3. RESULTS

3.1. *The Properties of the Data and the Identification of Emission Lines*

There are several aspects of the data that negatively impact our ability to identify genuine spectral features. Since we are observing in the slitless mode, each object produces zero-, first-, and second-order spectra. The first-order spectra contain the useful data, and the zero and second orders are sources of confusion; the zero-order images, as they can be mistaken for emission features, particularly when they fall on the first-order continua of other objects. The zero-order images are slightly dispersed, and for point sources often appear bimodal. The displacement between the zero-order images and the start of the first-order spectrum is 27″, or 135 pixels, a substantial fraction of the array size. For this reason the zero-order images are confined to roughly half of the detector area, and in most cases they can be identified by matching them with either the first-order spectra or with an object in the direct image. There is a small portion of the detector in which zero-order images can appear without either first-order spectra or images in the direct frame. In addition to the confusion caused by the zero-order images and second-order spectra, there are artifacts associated with hysteresis in the HgCdTe detectors. Bright stars imaged with the broadband filters just before a grism observation will produce a low level after-image that is displaced from the first-order spectrum. Since the data are nearly always taken in pairs of direct and grism exposures, these persistent images appear in multiple exposures and can take on the appearance of isolated emission lines. Strong cosmic-ray events have similar properties, but the two-position dithering sequence aids in their identification and removal. Particularly strong particle events effect more than 1 pixel and can produce amorphous clouds of electrons that decay over timescales of an orbit. During the South Atlantic Anomaly (SAA) passage, the particle event rate is quite large, and most NICMOS images or spectra obtained at this time are not usable. The hysteresis in the detectors often renders subsequent exposures useless as well. For a significant number of our short pointings, one of the two 896 s grism exposures has greatly enhanced noise from residual CR events associated with the SAA passage.

Given the wide variety of pointlike features that appear in the two-dimensional grism images, we have made our emission-line identifications on the basis of visual inspection. The eye can detect compact features to quite low signal-to-noise levels. To convince ourselves that any pos-

sible emission line was real, we proceeded to eliminate all possible false signals, zero-order images, persistent images, CRs, etc. To facilitate the detection of incompletely rejected cosmic rays and other noise features, we split each observation into two frames of equal length and compared the position of possible emission features. Those features that appeared in only one of the data sets, or did not move with the dither pattern, were rejected. In Figure 1 we show two pairs of F160W/G141 frames and mark examples of each of the sources of confusion, as well as real emission features.

3.2. *Areal Coverage and Depth*

During the period from 1997 October to 1998 October, 3500 camera 3 exposures were taken as part of the public and our crafted guest observer parallel programs. These contain a mix of direct exposures with the F160W and F110W filters and spectroscopic exposures with the G141 and G096 grisms. A total of 456 pairs of F160W/G141 frames were taken during this time. These were distributed in 107 independent pointings with exposure times ranging from 1790 to 21,480 s. The G141 grism spectra can provide useful data for our purposes to quite low Galactic latitudes. Rather than adopt a strict latitude cutoff, we chose to reduce all of the data and reject those with high stellar densities. After some experience we rejected all fields with stellar densities greater than 50 arcmin^{-2} above a 10 σ threshold in the F160W direct image. We are left with 85 pointings covering 64 arcmin^2.

The final depth achieved varied considerably from field to field. For the 1790 s exposures the noise level varied by a

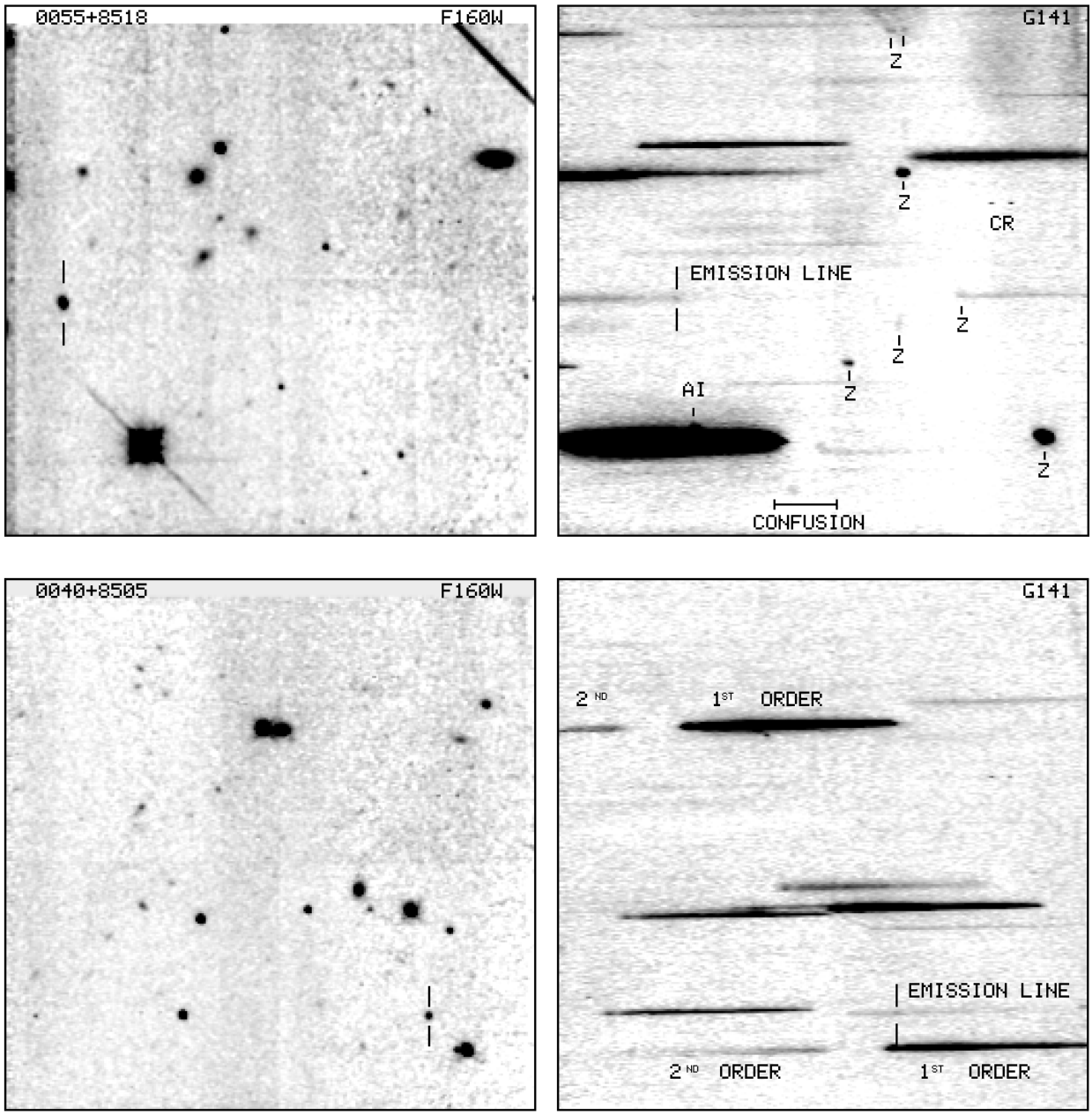

FIG. 1.—Two typical pairs of direct and two-dimensional grism images. Each field is 51″ × 51″ and oriented in arbitrary directions. In the G141 frames we have marked zero-order images (Z), residual after images (AI), persistent cosmic rays (CR), first- and second-order spectra, and our identified emission lines. The region marked as "confusion" (*top*) identifies the portion of the detector within which zero-order images neither have corresponding first-order spectra within the G141 field of view or direct images in the F160W field. We have marked the objects producing the emission lines in the F160W images.

factor 3. Some of this variation was due to genuine background variations, but much of it was due to various non-Poisson sources of noise (e.g., SAA passage). For longer pointings the depth increased roughly as the square root of the exposure time. We define our limiting depths as 3 σ within a 4 pixel (0.16 arcsec^2) aperture. This area is a reasonable representation of the area of the camera 3 PSF at the focus achieved outside of the campaign mode. In Figure 2 we show a histogram of the 3 σ, 4 pixel limits for the G141 data.

3.3. *Detected Emission Features*

In Table 1 we list all of the fields for which we have reduced and examined the G141 grism data. For each pointing we give the J2000 IAU designation, the Galactic latitude, and the exposure times for the F160W and G141 filters.

In Figure 1 we show two typical pairs of direct and two-dimensional grism images. These two grism images show many of the features discussed in the previous section (zero-order images, first- and second-order spectra, after images), as well as one emission-line object each. After careful examination of all of the spectra, we assembled a catalog of 33 emission-line detections. Table 2 gives the field names, object designation, J2000 coordinates, observed wavelengths, redshifts, line fluxes, significance levels, observed equivalent widths, and equivalent width limits (2 σ) for these 33 emission-line galaxies. We set a rejection threshold at 3 σ; the derived significance levels of our cataloged emission lines are given in Table 2. These 33 emission lines are distributed in 22 fields, six of which contain more than one emission-line object. We do not convincingly detect more than one line in any object. All of the lines are quite strong in terms of equivalent width. This is expected given the low spectral resolution of the grisms; weak lines against bright continua are not easily detected. The observed equivalent width limits reflect the signal-to-noise ratios in the continua, as well as the galaxy sizes. The 2 σ observed equivalent width limits are calculated as follows: $W_{\rm lim} = 2 \times [s/(S/N)] \times N^{1/2}$, with s the scale in angstroms per pixel, S/N the signal-to-noise ratio per pixel of the continuum at the emission line, and N the number of pixels under each line. For lines that are not velocity resolved, the apparent line width is the convolution of the instrumental spatial resolution and the intrinsic size of the emission-line region. For our emission-line galaxies, we take N to be 3 pixels. The 2 σ rest-frame equivalent width limits range from 9 to 130 Å, with an average of 40 Å. In Figure 3, we show direct images in the F160W band ($\sim H$ band) and two-dimensional grism spectra for all 33 emission-line galaxies. Figure 4 presents the extracted one-dimensional spectra of all 33 emission-line galaxies.

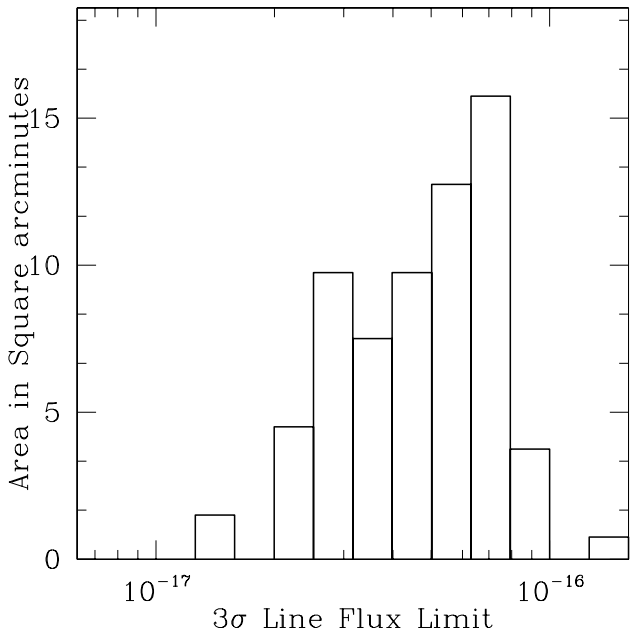

FIG. 2.—Histogram of the achieved 3 σ, 4 pixel noise levels in the G141 data. Each pointing covers 0.75 arcmin^2.

We believe that most, if not all, of the emission lines that we have detected are either Hα or an unresolved blend of Hα + [N II] $\lambda\lambda$6583, 6548. In Table 3 we list the line luminosities, star formation rates derived from the Kennicutt (Kennicutt, Bothun, & Schommer 1984; Kennicutt 1992) relation, the apparent H-band magnitudes (on the Vega scale), and $J-H$ colors for the fields where the F110W observations were available. The identification of the emission lines as Hα is based on a number of arguments. First, the most plausible identifications are Hα + [N II] $\lambda\lambda$6583, 6548, [O III] $\lambda\lambda$5007, 4959, Hβ λ4861, and [O II] λ3727. At the peak of the G141 transmission these correspond to redshifts of 1.28, 2.0, 2.1, and 3.0, respectively. Studies of nearby galaxies show that Hα + [N II] is usually the strongest line, the second being [O II] λ3727 (Kennicutt 1992). The equivalent width of Hβ scales with the equivalent width of Hα as $W(\mathrm{H}\beta) = 0.15W(\mathrm{H}\alpha) - 4$. Even in the bluest Magellanic irregular and starburst galaxies, W(Hβ) is only $\sim$5 Å. With a resolution of 5000 km s^{-1}, it would be quite difficult to detect such lines in our data. Redshifts of $\sim$3 are highly unlikely given the median F160W magnitude of 20.5, as shown in Figure 5. The $z \sim 3$ Lyman break galaxies have typical F160W magnitudes that are 2 magnitudes fainter ($H \sim 22.5$; Giavalisco et al. 1999). The space density of our emission-line objects is sufficiently large that they are unlikely to represent the extreme tail of the luminosity distribution of the $z \sim 3$ Lyman break objects. If not Hα, it is more likely that the lines that we see are [O III] $\lambda\lambda$5007, 4959, rather than [O II] λ3727. The [O III] $\lambda\lambda$5007, 4959 lines could be marginally resolved in our spectra, but only if the objects are spatially compact. At $z \sim 1.5$, if we take an $R-H$ color of 3, the median H magnitude of our objects corresponds to $M_R = -21.7$ for $H_0 = 50$ km s^{-1} Mpc^{-1}, $q_0 = 0.5$, quite close to M_R^* determined from the Las Campanas Redshift Survey (Lin et al. 1996). In Figure 6, the left-hand panel shows the distribution of Hα line luminosity; the median line luminosity is 2.5×10^{42} ergs s^{-1}, close to the value of $L^*_{\mathrm{H}\alpha}$ derived in local surveys (e.g., Gallego et al. 1997; Tresse & Maddox 1998). If the emission lines are actually [O III] $\lambda\lambda$5007, 4959, the implied rest-frame H-band luminosities and emission-line luminosities would be a factor of 2.5–3 larger and the likelihood of such objects appearing in flux-limited samples is suppressed by the exponential cutoff in the luminosity function. Strong [O III] $\lambda\lambda$5007, 4959 emission is more often identified with active galactic nuclei (AGNs) than star-forming galaxies, making it even less likely that [O III] emitters at $z \sim 2$ dominate our detections (see § 4). Furthermore, in the redshift range between 1.6 and 1.8, both [O III] $\lambda\lambda$5007, 4959 and [O II] λ3727 are visible in the G141 passband. Lines

TABLE 1

THE NICMOS GRISM SURVEY FIELDS

Field	$\|b\|$	F160W	G141	Field	$\|b\|$	F160W	G141	Field	$\|b\|$	F160W	G141	Field	$\|b\|$	F160W	G141
J0002−1531.....	73	2550	5370	J0535−0519.....	19	510	1790	J1120+2328.....	69	510	1790	J1604+4318.....	48	3830	5370
J0017+1544.....	46	1020	1790	J0535−0623.....	19	5100	14320	J1120+2324.....	69	3570	12530	J1612+6539.....	40	510	1790
J0022−7202.....	44	510	1790	J0540−6939.....	31	2550	3580	J1120+1300.....	64	16860	10740	J1633−6732.....	13	1530	5370
J0023−7209.....	44	1530	1790	J0543−6909.....	31	1530	1790	J1129+5832.....	55	510	1790	J1633−0941.....	24	2550	8950
J0029+8516.....	22	1020	1790	J0547−7004.....	30	510	1790	J1133+0403.....	60	510	1790	J1642+3944.....	41	510	1790
J0040+8457.....	22	1530	1790	J0548−5101.....	30	510	1790	J1134+0406.....	60	510	1790	J1701−2143.....	12	1020	3580
J0040+8505.....	22	510	1790	J0551+1552.....	05	2550	3580	J1143−8036.....	18	1000	1917	J1726−4821.....	07	2338	6136
J0050−5207.....	65	2040	1790	J0551+1549.....	05	510	1790	J1145+4733.....	65	2550	8950	J1741−0701.....	12	510	1790
J0051+8523.....	22	510	1790	J0609+2415.....	02	2040	1790	J1145+4735.....	65	1510	1917	J1744−2900.....	00	510	1790
J0055+8518.....	22	3060	10740	J0613+4752.....	13	510	1790	J1146+4723.....	66	1530	3580	J1752−1739.....	04	2040	1790
J0056+8510.....	22	510	1790	J0622−0018.....	06	1530	5370	J1151+5509.....	59	1031	2428	J1753−1739.....	04	1020	3580
J0100−7213.....	44	1020	3580	J0627−6512.....	26	1020	1790	J1153+4917.....	65	510	1790	J1755−2158.....	01	510	1790
J0100−7212.....	44	2295	8055	J0655+7910.....	26	2040	7160	J1218+4714.....	68	3570	7160	J1755−2200.....	01	510	1790
J0100−7213.....	44	1785	6265	J0709+4840.....	22	510	1790	J1226+3335.....	81	510	1790	J1758+6715.....	29	1530	3580
J0107+3230.....	30	510	1790	J0738+0507.....	12	1530	5370	J1228+4410.....	72	510	1790	J1802−2330.....	00	510	1790
J0133+3028.....	31	510	1790	J0741+6515.....	29	1031	2428	J1236+6225.....	54	510	1790	J1822+1511.....	13	1020	3580
J0133+3026.....	31	510	1790	J0804+0510.....	18	1020	1790	J1237+6219.....	54	6120	21480	J1822+1512.....	13	1020	3580
J0138−1749.....	75	510	1790	J0808+7459.....	31	1510	1917	J1237+6215.....	54	4590	16110	J1822+1512.....	13	510	1790
J0143+3259.....	28	1020	3580	J0809+7608.....	30	510	1790	J1237+6210.....	54	1530	5370	J1824−3020.....	08	2040	3580
J0233−0231.....	55	510	1790	J0811+7505.....	31	510	1790	J1238−4954.....	12	5100	10740	J1847−0451.....	01	510	1790
J0234+0340.....	50	510	1790	J0851+1151.....	32	1660	1790	J1238−4954.....	12	2040	7160	J1900−3637.....	17	1020	1790
J0234+0350.....	50	1020	3580	J0911−6457.....	11	510	1790	J1238−4954.....	12	1530	5370	J1912−5948.....	25	1031	2428
J0238+1634.....	39	2550	8950	J0917+8142.....	31	510	1790	J1256+2204.....	84	1020	1790	J1917−3330.....	19	1020	3580
J0240−0141.....	53	1020	3580	J0920+6909.....	38	510	1790	J1301+5900.....	58	510	1790	J1938−1621.....	17	510	1790
J0240−0140.....	53	1530	5370	J0922+8136.....	32	510	1790	J1316+2911.....	84	510	1790	J1958+4039.....	05	5100	14320
J0318−6632.....	44	510	1790	J0923+8137.....	32	510	1790	J1326−4258.....	19	510	1790	J1958+4037.....	05	4080	10740
J0325−3618.....	56	1020	3580	J0923+8149.....	32	510	1790	J1326−4245.....	19	510	1790	J2000+2236.....	03	510	1790
J0349+1712.....	28	1530	1790	J0927−0502.....	31	1530	5370	J1336+5150.....	63	1530	3580	J2044−3124.....	36	2040	5370
J0354+0945.....	32	1020	3580	J0931−0450.....	32	510	1790	J1336−2959.....	31	1020	3580	J2044+6758.....	15	255	895
J0400−4433.....	48	1020	3580	J0931−0449.....	32	510	1790	J1337+7023.....	46	2040	1790	J2044+6758.....	15	1275	895
J0408−1207.....	41	510	1790	J0950+7222.....	38	510	1790	J1338+7009.....	46	510	1790	J2056−0443.....	29	1530	1790
J0408−1209.....	41	510	1790	J0954+6905.....	40	1318	2556	J1341+2824.....	78	4080	14320	J2106−2411.....	39	2040	3580
J0421+1926.....	21	1530	1790	J0955+6908.....	40	1510	1917	J1343+0218.....	62	510	1790	J2144+2813.....	18	510	1790
J0424+2707.....	15	510	1790	J0956+6937.....	40	1530	3580	J1343+0124.....	61	1020	3580	J2150+2845.....	19	1530	5370
J0425+1709.....	21	510	1790	J1020+3654.....	56	1020	3580	J1343+0225.....	62	510	1790	J2151+2854.....	19	1020	3580
J0430+2449.....	15	510	1790	J1039+4313.....	58	510	1790	J1345+0201.....	61	1020	3580	J2155+6334.....	07	1530	1790
J0431+1803.....	20	1530	3580	J1039+4145.....	59	6380	3580	J1346+0206.....	61	510	1790	J2155+6341.....	07	1530	3580
J0432+2424.....	15	1020	1790	J1044−5936.....	00	1530	1790	J1347+0219.....	61	1020	3580	J2155+6343.....	07	1530	3580
J0433+2526.....	15	510	1790	J1044−5948.....	00	3060	7160	J1402+5419.....	59	510	1790	J2156+6345.....	07	2040	1790
J0443+3612.....	06	1530	3580	J1053−0342.....	48	1530	5370	J1415+1910.....	69	2040	5370	J2157+6331.....	06	1318	2556
J0455+3029.....	08	510	1790	J1055−0418.....	48	1020	1790	J1432+0423.....	56	1530	5370	J2157+6338.....	07	7140	5370
J0458−0404.....	26	510	1790	J1056−0337.....	48	1020	3580	J1454+1218.....	57	510	1790	J2217−0336.....	46	510	1790
J0506+5250.....	07	2040	3580	J1057−0318.....	48	2040	5370	J1504+0110.....	48	510	1790	J2240+8031.....	19	510	1790
J0526−6602.....	33	2550	3580	J1120+2327.....	69	510	1790	J1507+0234.....	49	1530	5370	J2257+2050.....	34	510	1790
												J2319+0809.....	48	1020	3580

TABLE 2

EMISSION-LINE OBJECTS FROM THE NICMOS GRISM SURVEY

Field	Object	α(2000)	δ(2000)	λ (μm)	$z_{H\alpha}$	Flux[a] (ergs s^{-1} cm^{-2})	N_σ	W_{obs} (Å)	W_{lim}[b] (Å)
J0040+8505.....	a	00 40 43.93	85 05 49.4	1.727	1.63	1.5	4.8	250	62
J0055+8518.....	a	00 55 37.85	85 18 17.3	1.160	0.76	5.3	5.2	240	25
J0240−0140.....	a	02 40 10.85	−01 40 53.0	1.839	1.80	0.7	12	160	49
J0613+4752.....	a	06 12 59.93	47 52 43.3	1.341	1.04	1.3	5.8	60	60
J0622−0018.....	a	06 22 13.78	−00 18 25.5	1.402	1.14	2.9	4.0	403	55
J0627−6512.....	a	06 27 32.20	−65 12 35.0	1.742	1.65	1.8	3.5	176	86
J0738+0507.....	a	07 38 57.86	05 07 35.2	1.210	0.84	16	10.9	161	32
	b	07 38 58.37	05 07 56.7	1.77	1.69	0.9	3.0	180	105
J0741+6515.....	a	07 41 40.89	65 15 23.8	1.612	1.45	1.0	7.4	92	72
	b	07 41 45.37	65 15 36.2	1.879	1.86	1.8	12.8	165	118
	c	07 41 44.67	65 15 06.9	1.33:	1.06	1.8	4.1	879	101
J0917+8142.....	a	09 17 47.25	81 42 21.4	1.880	1.86	2.9	9.4	375	131
	b	09 17 44.96	81 42 40.6	1.883	1.87	0.9	4.4	224	87
	c	09 17 39.64	81 43 06.5	1.364	1.07	56	115	737	32
J0923+8149.....	a	09 23 34.32	81 50 11.2	1.572	1.39	4.2	7.0	547	114
J0931−0449.....	a	09 31 25.97	−04 49 45.4	1.299	0.98	24	14.4	550	49
J1039+4145.....	a	10 39 41.79	41 45 04.4	1.636	1.49	1.8	10.7	410	118
J1056−0337.....	a	10 56 56.41	−03 37 03.9	1.126	0.72	4.6	3.1	168	36
J1120+1300.....	a	11 20 37.36	13 00 07.1	1.376	1.10	0.2	6.8	2809	60
J1120+2323.....	a	11 20 24.29	23 22 40.8	1.557	1.37	1.9	4.8	660	74
	b	11 20 22.36	23 23 13.0	1.397	1.13	1.4	4.8	456	83
J1134+0406.....	a	11 34 04.71	04 06 33.7	1.260	0.92	5.4	3.2	1165	86
J1143−8036.....	a	11 43 19.56	−80 36 46.2	1.538	1.35	1.2	5.5	310	80
	b	11 43 19.73	−80 36 46.9	1.549	1.36	0.7	5.4	330	53
	c	11 43 10.31	−80 37 06.9	1.668	1.54	1.2	3.8	353	73
	d	11 43 18.46	−80 36 30.2	1.49	1.27	1.3	4.1	377	298
J1145+4733.....	a	11 45 29.14	47 33 35.2	1.257:	0.92	1.1	2.5	250	184
J1218+4714.....	a	12 18 36.42	47 14 34.0	1.56	1.38	0.7	3.9	108	36
J1237+6209.....	a	12 37 49.04	62 09 50.0	1.802	1.74	0.9	5.2	172	51
J1237+6215.....	a	12 37 38.85	62 15 24.8	1.778	1.71	0.4	3.2	108	24
J1237+6219.....	a	12 37 06.57	62 19 37.1	1.557	1.37	1.8	6.0	607	65
	b	12 37 05.28	62 19 38.5	1.348	1.05	1.3	2.8	546	164
	c	12 37 07.71	62 19 24.8	1.734	1.64	0.4	4.2	580	303

NOTE.—Units of right ascension are hours, minutes, and seconds, and units of declination are degrees, arcminutes, and arcseconds.

[a] The Hα line flux is in units of 10^{-16} ergs s^{-1} cm^{-2}.

[b] W_{lim} is the 2 σ observed equivalent width limit, which reflects the signal-to-noise ratio of the continuum near the wavelength of the Hα line.

with longer rest wavelengths are possible, but unlikely, identifications. He II 10830 implies redshifts that are implausibly low ($\sim$0.38), and for most redshifts both of the [S III] $\lambda\lambda$9069, 9545 lines would be within the passband. Teplitz, Malkan, & McLean (1999b) have confirmed the identification of Hα in two of our objects (J0055+8518a, $z = 0.76$; J0622−0018a, $z = 1.12$) by detecting [O II] λ3727 at the appropriate redshifts in spectra taken with LRIS on the Keck 10 m telescope.

Hα is blended with [N II] $\lambda\lambda$6583, 6548 in our spectra. To correct for the contribution from the [N II] doublet, we adopted [N II] λ6583/Hα = 0.3, the average ratio for all types of galaxies in the Gallego et al. (1997) objective-prism survey. Taking [N II] λ6583/[N II] λ6548 = 3, we have $f(\mathrm{H}\alpha) = 0.71 \times f(\mathrm{H}\alpha + [\mathrm{N\ II}])$. Thus the correction to the estimated star formation rates in Table 3 is 29%. We have not applied any extinction corrections to either the Hα luminosities or the star formation rates.

3.4. *Notes on Individual Fields*

In Figure 3 we present cutout images and two-dimensional spectra of all of our emission-line candidates. Flux and wavelength-calibrated one-dimensional spectra are shown for the same objects in Figure 4. We designate each object by its IAU J2000 field designation and a letter. There are a few fields that have noteworthy features, and we detail these below.

0040+8505A.—This is one of the weaker lines, in terms of W_λ, in our sample. There are only two exposures of this field, but the emission feature is seen in both frames.

0613+4752A.—The emission line in this object is more compact than the continuum. As in the case of 0040+8505, there are only two exposures for this field, but the narrow emission feature is seen in both frames and moves with the dither pattern.

0622−0018A.—This low-redshift object is detected in a very low latitude field ($b = -6°$). The emission line is spatially extended and appears to follow the continuum distribution as revealed in the F160W image.

0738+0507A.—This is also a low-latitude field, and the object in question is the brightest in our sample. The large equivalent width and compact morphology of the emission line suggests that this object might be an AGN.

0738+0507B.—The putative emission line is quite faint

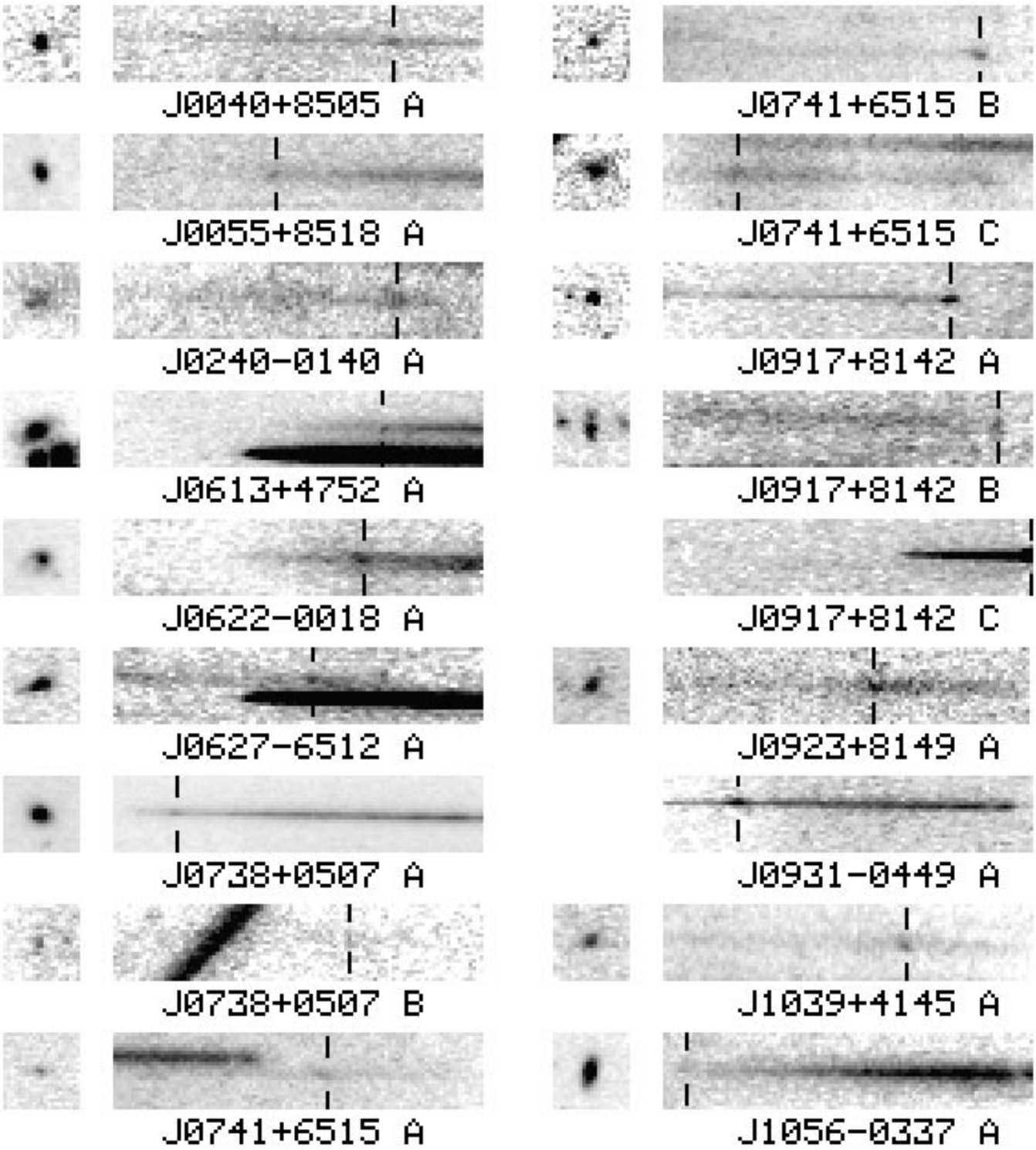

FIG. 3.—Mosaic of F160W band direct images and two-dimensional grism spectra of 33 emission-line galaxies found in our survey. The emission lines in each object are marked with vertical ticks. For a few of the objects the continuum images fall near the edge or just off the edge of the F160W field of view. For these objects (0917 + 8142C, 0931 − 0449A) we do not have F160W images.

and diffuse. There are six exposures of this field, and the emission feature appears with equal strength in the two independent subsets of the data.

0741+6515A.—The emission line in this object is spatially resolved, and its morphology is similar to that of the continuum shown in the F160W image.

0741+6515B.—The emission line in this object is at the extreme red end of the continuum spectrum and is spatially offset from the continuum. The emission feature is located in a portion of the field such that it cannot be a zero-order artifact.

0917+8142A.—This emission feature is also at the extreme red end of the continuum. At the location of this feature there is the possibility of zero-order images. If this feature were a zero-order image, the object would be just off the edge of the F160W direct image. The first-order contin-

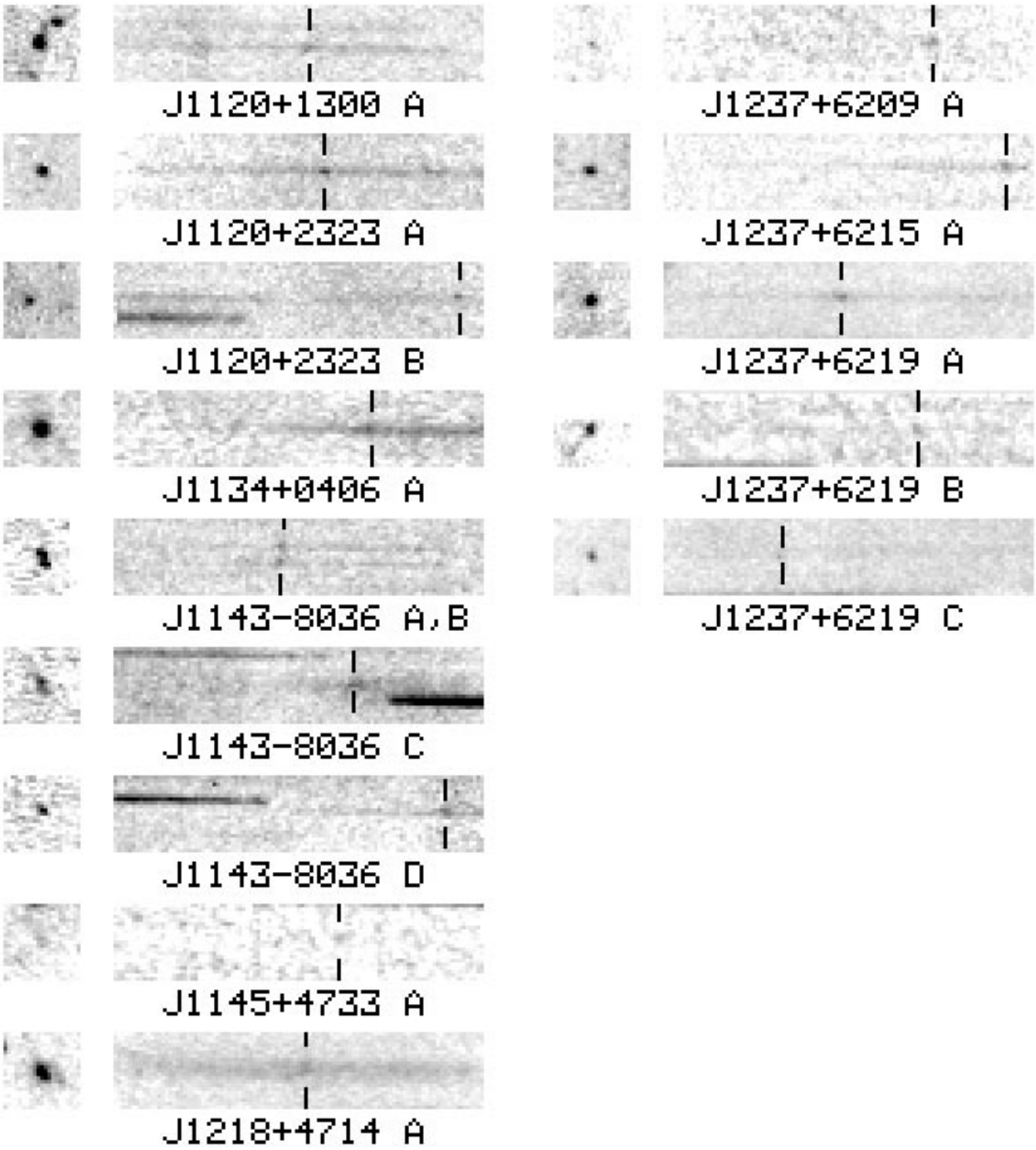

FIG. 3.—*Continued*

uum of a zero-order image at this location would be partially on the G141 frame, but there is a confusing signal from a bright galaxy at this location. The spatial coincidence between the continuum and emission features led us to classify this as a real emission line, although this object should be considered less secure than the others.

0917+8142C.—The putative emission line in this object is at the edge of the G141 field of view. The feature is only present in one of the two dithered frames, and it was moved off the detector by the 2″ dither motion. The object is also located just outside the F160W field in both dither positions. The great strength of this line makes it a candidate AGN.

1120+2323A, B.—The two emission lines in this field are extremely compact. Both emission features are seen in the two dither positions. For reasons that are not entirely clear, the focus in this particular set of exposures was unusually good. The difference may have arisen from breathing of the telescope optical assembly, or from motions within the NICMOS Dewar.

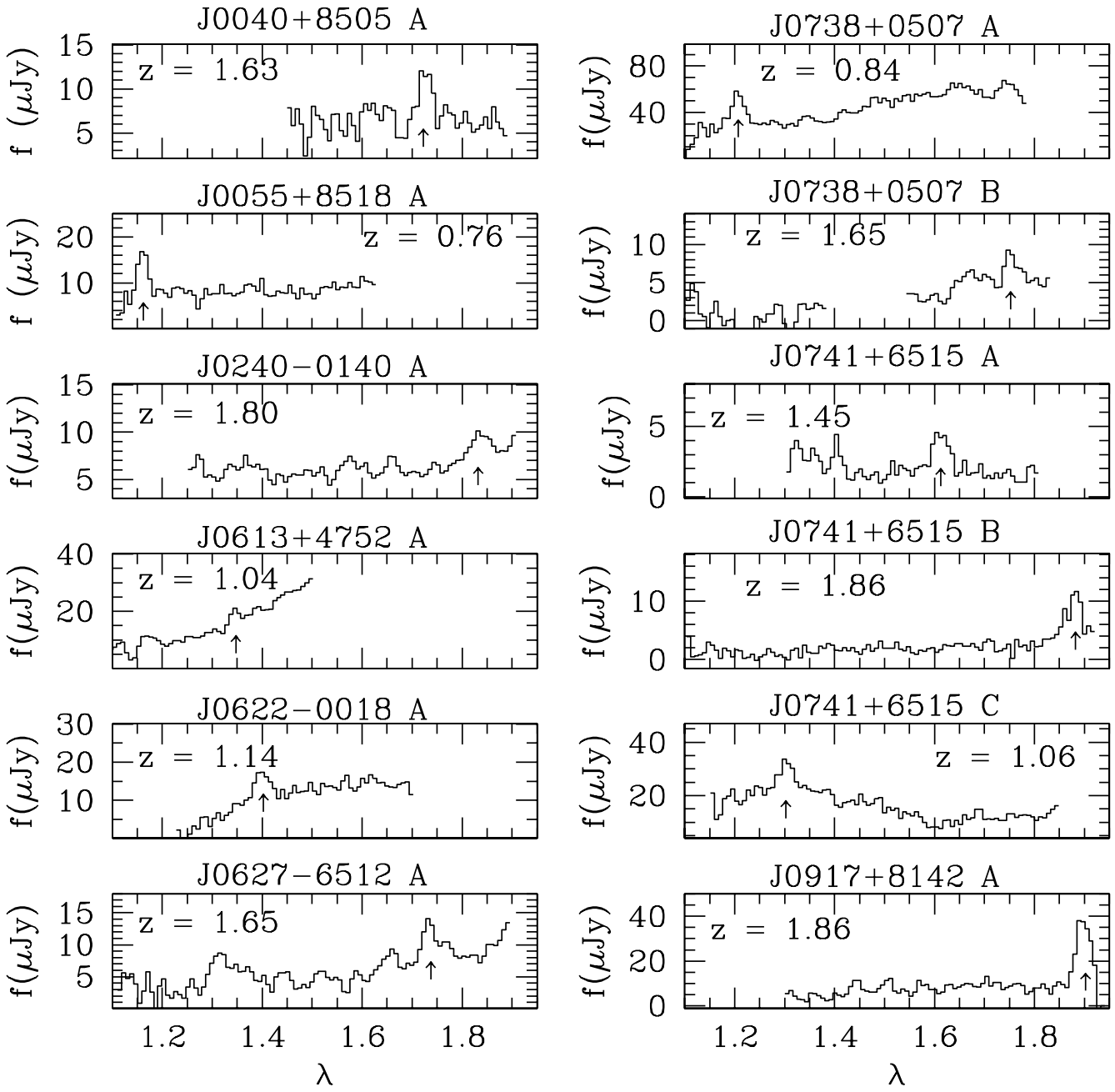

FIG. 4.—Extracted one-dimensional spectra of the emission-line galaxies. For each object we have marked our candidate emission lines with arrows below the line. We plot the entire range of the G141 grism for each spectrum even though parts of the spectrum have fallen beyond the field of view of the detector for several objects. The redshifts, assuming an Hα identification for the line, are given for each object. There are deficiencies in the background removal for several objects that lead to significant uncertainties and rollovers in the continuum level (e.g., 1237 + 6215A). There are edges in the spectra of objects for which a portion of the spectrum falls beyond the edge of the detector (e.g., 0040 + 8505a). The gap in the spectrum of 0738 − 0507B is due to scattering of light from a bright star (see Fig. 3).

1143−8036A, B.—This pair of emission-line galaxies appears to have nearly identical redshifts in the two-dimensional G141 frame. The slightly different locations in the F160W image result in different wavelength scales, and hence different redshifts. The close proximity of the two images make accurate centroiding of the F160W images difficult, and this introduces uncertainties into the wavelength calibrations.

4. DISCUSSION

This survey provides a unique window on galaxies at intermediate redshifts. In so doing it provides us with a view of the bright end of the Hα luminosity function averaged over a cosmologically significant volume. From these data we will derive an Hα luminosity function and a measure of the volume-averaged star formation rate that is fairly insensitive to the effects of extinction. These analyses require careful treatment of the selection efficiencies and biases inherent in a slitless low-resolution survey and are presented in Yan et al. (1999). In the present work we restrict ourselves to a first-order census of bright emission-line objects and a brief comparison with other surveys in this redshift range.

There are a number of near-IR emission-line imaging

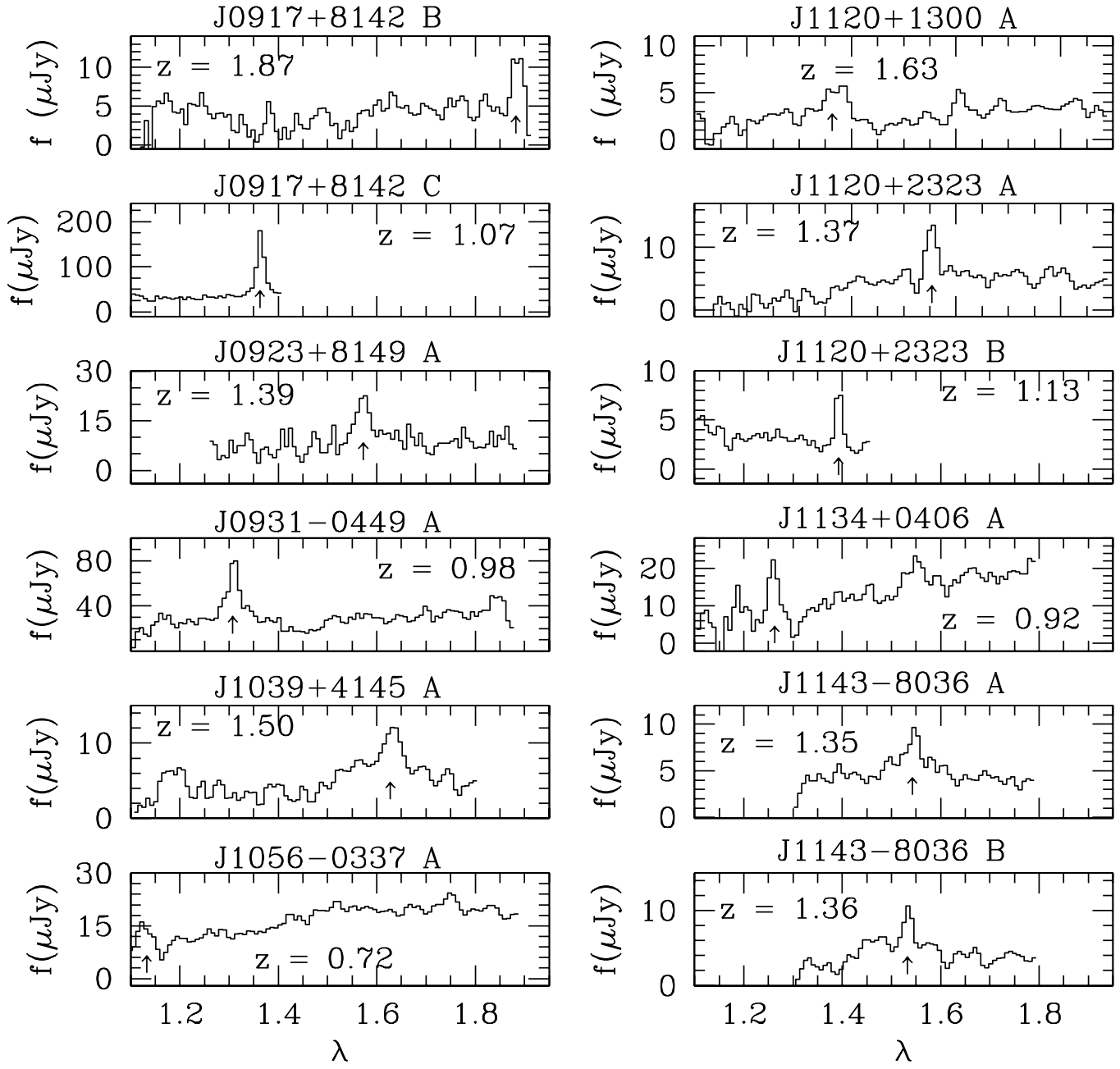

FIG. 4.—*Continued*

surveys that are either in progress or have been recently completed. In Table 4 we compare the characteristics of our survey with several ground-based programs. Clean comparisons are difficult since our survey is of a different character and spans a very wide range of exposure times from field to field. In our deepest pointings we achieve flux limits that are substantially deeper than the narrowband imaging survey being carried out by Teplitz et al. (1999a) with the Keck telescope. Our median and area-weighted sensitivities are both 4.1×10^{-17} ergs cm^{-2} s^{-1} (3 σ, 4 pixels), $\sim$60% deeper than the area-weighted detection limit reported by Teplitz et al. (1999a). The two principal differences between our survey and those listed in Table 4 are the volumes probed and the choice of sight lines. Because our survey is spectroscopic we are able to probe large columns in the z-direction. The comparable areal coverage of our survey then leads to total comoving volumes that are 1–2 orders of magnitude larger than those surveyed by the narrowband imaging programs.

Inspection of Table 4 reveals that most of the narrowband imaging surveys are targeted at lines of sight and redshifts that are a priori known to contain either luminous galaxies or absorption-line systems. The motivation for this can be clearly seen in the results of the first Calar Alto survey (Thompson et al. 1996). Surveys along sight lines without absorbers, or in completely random areas, yield few strong line emitters in the volumes that can be probed by imaging with 1% filters. Thompson et al. (1996) detected a single object in 30,000 h_{50}^{-3} Mpc^3, implying a space density of 3×10^{-5} h_{50}^3 Mpc^{-3}. The choice of AGN and/or absorber redshifts is effective in producing detections, but it clearly impacts the inferred space density of line emitters. Teplitz et al. (1999a), targeting a mix of QSO and absorber redshifts, report the highest space density at approximately

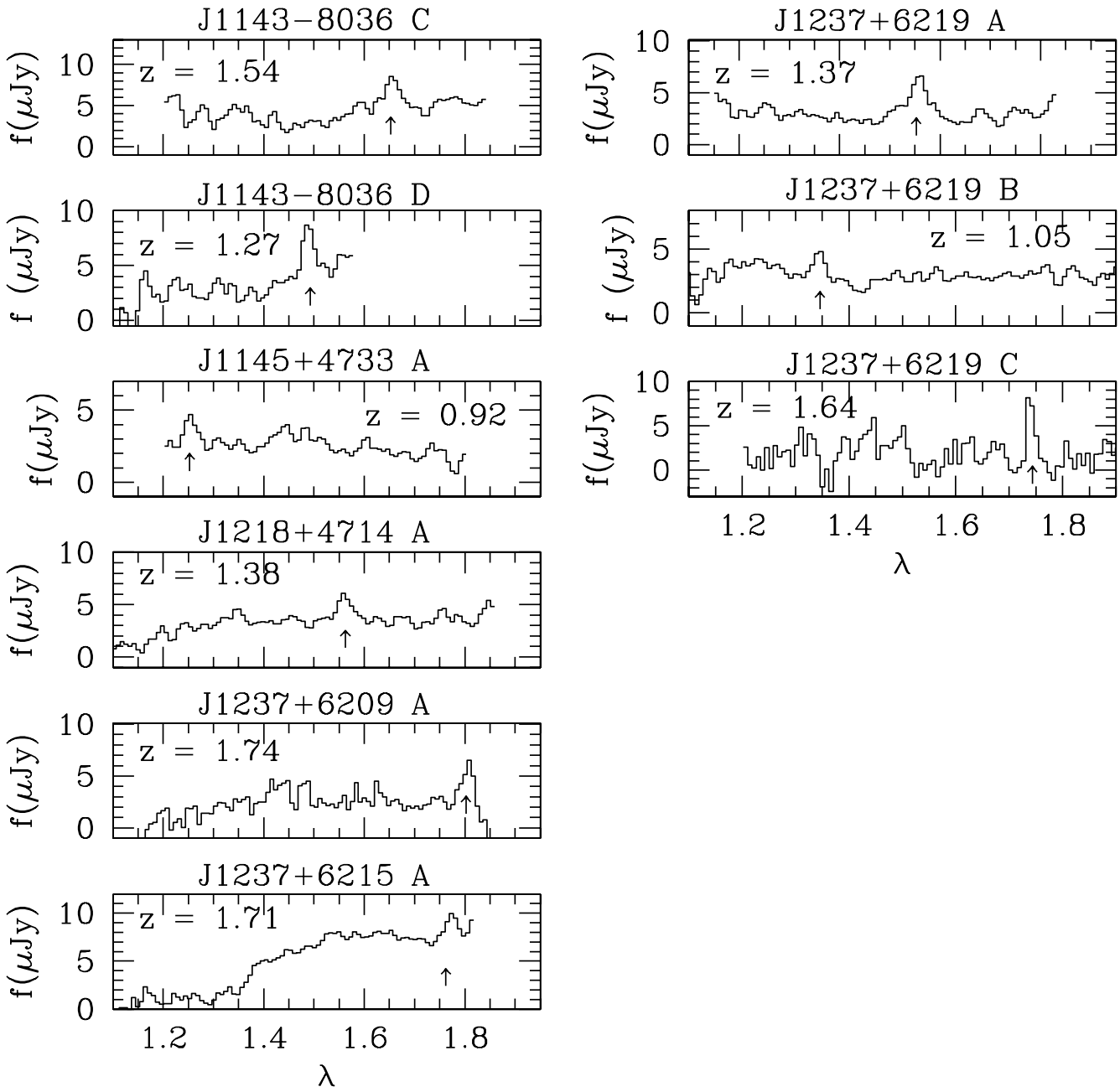

FIG. 4.—*Continued*

$10^{-2}\ h_{50}^{3}$ Mpc^{-3}. This is quite different from the results of the Thompson et al. (1996) survey, even when allowing for the very different depths of the two surveys. The second Calar Alto survey (Mannucci et al. 1998) demonstrates the effect of targeting metal line absorption systems, while Bechtold et al. (1998) have achieved similar results using damped Lyα redshifts.

Our Hα survey probes an effective comoving volume of $1.0 \times 10^{5}\ h_{50}^{-3}$ Mpc^{3} ($2.1 \times 10^{5}\ h_{50}^{-3}$ Mpc^{3} for $q_0 = 0.1$). Thus the comoving number density of emission-line galaxies averaged over our volume is $3.3 \times 10^{-4}\ h_{50}^{3}$ Mpc^{3}. In comparison, the present-day comoving number density of galaxies brighter than L^* in the B band is $7 \times 10^{-4}\ h_{50}^{3}$ Mpc^{-3} (Ellis et al. 1996), and the bright Lyman break galaxies at $z \sim 3$ reported by Steidel et al. (1996) have a space density of $3.6 \times 10^{-4}\ h_{50}^{3}$ Mpc^{-3}. The duty cycle of strong Hα emission in galaxies with bursting or variable star formation histories can be quite low given the sensitivity of strong line emission to only the most recent star formation. Thus it is not unreasonable that our space density is below that of present-day L^* galaxies and comparable to that of the UV continuum–selected galaxies at high redshift. The low resolution of the NICMOS grisms imprints a strong selection effect against emission lines with low equivalent widths. Given the incompleteness at low equivalent widths and the rather bright H-band magnitudes of the detected emission-line objects, it seems likely that we are sampling star formation in a population that is closely related to the majority population of massive galaxies.

The average star formation rate in our sample is 30 $M_{\odot}$ yr^{-1} (40 $M_{\odot}$ yr^{-1} for $q_0 = 0.1$). After correcting for [N II] contamination, this rate is reduced to 21 $M_{\odot}$ yr^{-1}. We have

TABLE 3

PHOTOMETRY OF EMISSION-LINE OBJECTS

Field	Object	$z_{H\alpha}$	H (mag)	$J-H$ (mag)	$\log_{10}(L_{H\alpha})$ (ergs s^{-1})	SFR ($M_\odot$ yr^{-1})
J0040+8505.....	a	1.63	20.4	...	42.40	22
J0055+8518.....	a	0.76	19.7	...	42.20	14
J0240−0140.....	a	1.80	20.8	1.1	42.16	13
J0613+4752.....	a	1.04	18.1	...	41.90	7
J0622−0018.....	a	1.14	19.1	...	42.34	19
J0627−6512.....	a	1.65	20.4	0.8	42.49	27
J0738+0507.....	a	0.84	17.9	...	42.78	54
	b	1.69	22.0	...	42.21	14
J0741+6515.....	a	1.45	21.1	0.8	42.10	11
	b	1.86	22.3	0.7	42.60	36
	c	1.06	19.6	1.0	42.06	10
J0917+8142.....	a	1.86	20.2	...	42.81	58
	b	1.87	20.2	...	42.31	18
	c	1.07	...	...	43.56	324
J0923+8149.....	a	1.39	19.1	...	42.69	44
J0931−0449.....	a	0.98	19.0	0.7	43.11	115
J1039+4145.....	a	1.49	20.2	1.4	42.39	22
J1056−0337.....	a	0.72	18.8	1.1	42.10	11
J1120+1300.....	a	1.10	20.8	0.6	41.14	1
J1120+2323.....	a	1.37	20.5	...	42.33	19
	b	1.13	21.1	...	42.01	9
J1134+0406.....	a	0.92	19.9	1.0	42.40	22
J1143−8036.....	a	1.35	21.4	...	42.11	12
	b	1.36	20.5	...	41.89	7
	c	1.54	20.8	...	42.24	16
	d	1.27	21.0	...	42.09	11
J1145+4733.....	a	0.92	...	...	41.71	5
J1218+4714.....	a	1.38	20.3	0.9	41.90	7
J1237+6209.....	a	1.74	23.3	0.5	42.24	15
J1237+6215.....	a	1.71	20.8	1.0	41.87	7
J1237+6219.....	a	1.37	20.5	...	42.31	18
	b	1.05	21.9	...	41.91	7
	c	1.64	22.3	...	41.83	6

NOTE.—The Hα luminosities and star formation rates were calculated for $H_0 = 50$ km s^{-1} Mpc^{-1} and $q_0 = 0.5$. Here the listed star formation rates have not been corrected for contamination from [N II] λλ6584, 6548. As described in detail in the text, the correction to the star formation rates is 29%. We only have $J-H$ colors for some of the fields where the F110W observations were available. Ellipses indicate no measurements.

not applied any extinction correction to the calculations of Hα luminosities and star formation rates. While our sample is not magnitude limited, the distribution of apparent magnitudes is sufficiently narrow to allow a reasonable comparison with magnitude-limited samples. As noted above, our median F160W magnitude of 20.5 is quite close to M_R^* as derived locally. It is interesting to note that the average star formation rate in the Lyman break objects before corrections for extinction are ~ 8 $M_\odot$ yr^{-1}, and that the extinction-corrected rates are a factor of 3–7 higher. Recent near-infrared spectroscopy of eight CFRS galaxies at $z \sim 1$ by Glazebrook et al. (1998) reached an Hα luminosity of 2×10^{42} ergs s^{-1} cm^{-2} with a star formation rate of 22 $M_\odot$ yr^{-1}, comparable to what we find, although our survey covers a wider range of Hα luminosities and star formation rates.

One source of uncertainty in using our data to derive global star formation rates is the unknown degree of contamination from AGNs. The fraction of AGNs in our sample could, in principle, be calculated using the AGN luminosity function in the redshift range from 0.7 to 1.9. However, at $z = 1.5$, an H magnitude of 20.5 corresponds roughly to an absolute B magnitude of -22.5, adopting a $B-H$ color similar to that for QSOs observed by Neugebauer et al. (1986). At this faint magnitude, the quasar luminosity function is completely unknown. The most recent quasar luminosity function at $z \sim 0.5$–2.0 reaches only to $M_B \sim -25$ (Hewett, Foltz, & Chaffee 1993). Furthermore, our knowledge of the Seyfert luminosity function is entirely based on local samples, and the degree of luminosity evolution in the Seyfert galaxy populations as a function of redshift is unknown. A crude estimate of the fraction of AGNs in faint redshift surveys can be derived from spectrophotometry of the CFRS sample. Using various emission-line ratios, Hammer et al. (1997) and Tresse et al. (1996) estimated that about 8%–17% of their galaxies at $z < 0.7$ are active galaxies, either Seyfert 2 or LINERs. A contamination rate at this level is consistent with our classification of two of our objects as candidate AGNs on the basis of their large equivalent widths and compact morphologies. If we exclude the two AGN candidates, the average star formation rate is 28.5 $M_\odot$ yr^{-1}, and 20 $M_\odot$ yr^{-1} if we correct the [N II] λλ6583, 6548 contamination. The impact of line misidentifications is comparable to that of the AGNs, as the

TABLE 4

EMISSION-LINE SURVEYS IN THE NEAR-IR

Site	Type	$\delta\lambda$	Area (arcmin^2)	Volume (Mpc^3)	z-Range	$f_{\rm lim}$ [a] (ergs s^{-1} cm^{-2})	$L_{\rm lim}$ [b] (ergs s^{-1})	N[c]	Reference	Remarks
Calar Alto 1	Imaging	1%	276	30000	2.05–2.65	3.4	9.4–15	1	1	Targeted toward AGN
Calar Alto 2	Imaging	1%	228	20600	0.9–2.4	2.4	1.0–9.5	18	2	QSO metal line absorbers
Keck/NIRC	Imaging	1%	11	815	2.3–2.5	0.7	2.5–3.2	13	3	QSO emission and absorbers
ESO near-IR	Imaging	1%	48	10000	2.2–2.3	1.9	6.2–6.8	2	4	Radio galaxies
Lick/UCLA camera.....	Imaging	1%	180	4255	0.9–1.0	3.9	1.8–3.3	2	5	QSO emission z
NICMOS parallel.....	Grism	45%	58	100000	0.8–1.9	0.4	0.1–0.9	33	6	Random fields

NOTE.—Comoving volumes are calculated for $H_0 = 50$ km s^{-1} Mpc^{-1} and $q_0 = 0.5$.

[a] All of the flux limits are 3 σ and in units of 10^{-16} ergs s^{-1} cm^{-2}.

[b] The luminosity limits represent the minimum line luminosities that the surveys are sensitive to and are in units of 10^{42} ergs s^{-1}.

[c] Number of emission-line galaxies found in the survey.

REFERENCES.—(1) Thompson et al. 1996. (2) Mannucci et al. 1998. (3) Teplitz et al. 1999a. (4) van der Werf et al. 1997. (5) Teplitz et al. 1999c. (6) This paper.

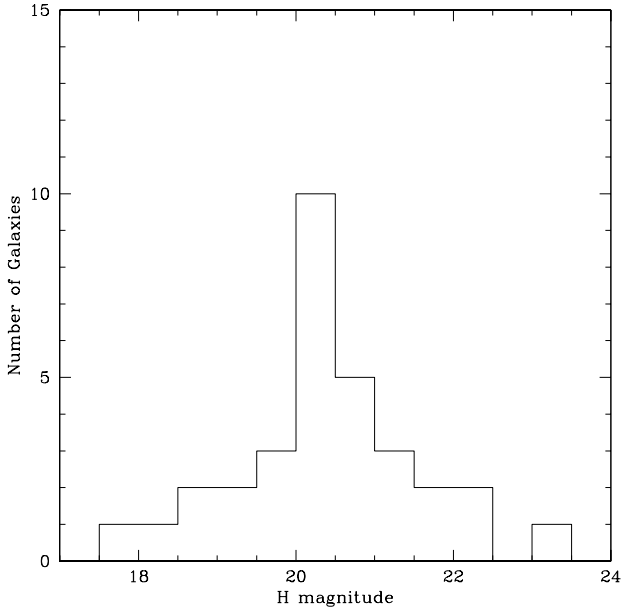

FIG. 5.—Distribution of apparent H magnitude of emission-line galaxies. The magnitudes are on the Johnson system.

most likely contaminants are [O III] $\lambda\lambda$5007, 4959 emission from compact nonstellar sources.

5. SUMMARY

We have presented the basic data derived from a spectroscopic survey of field galaxies in the near infrared. The G141 grism on NICMOS provides a unique opportunity to survey large volumes to faint flux levels in Hα and other emission lines. Our survey of 64 arcmin^2 at high and intermediate Galactic latitudes resulted in the detection of 33 emission-line objects, and we believe that most or all of these are Hα at redshifts between 0.75 and 1.9. The line luminosities, equivalent widths, and continuum magnitudes suggest that we are seeing active star formation in galaxies from the upper end of the luminosity function. The apparent space density of Hα emitters in our survey is similar to that of the bright Lyman break objects identified at $z > 3$ and is within a factor of ~ 2 of that of present day L^* galaxies. The grisms on NICMOS provide a first look at the enormous potential of low-resolution, near-IR spectroscopy from space.

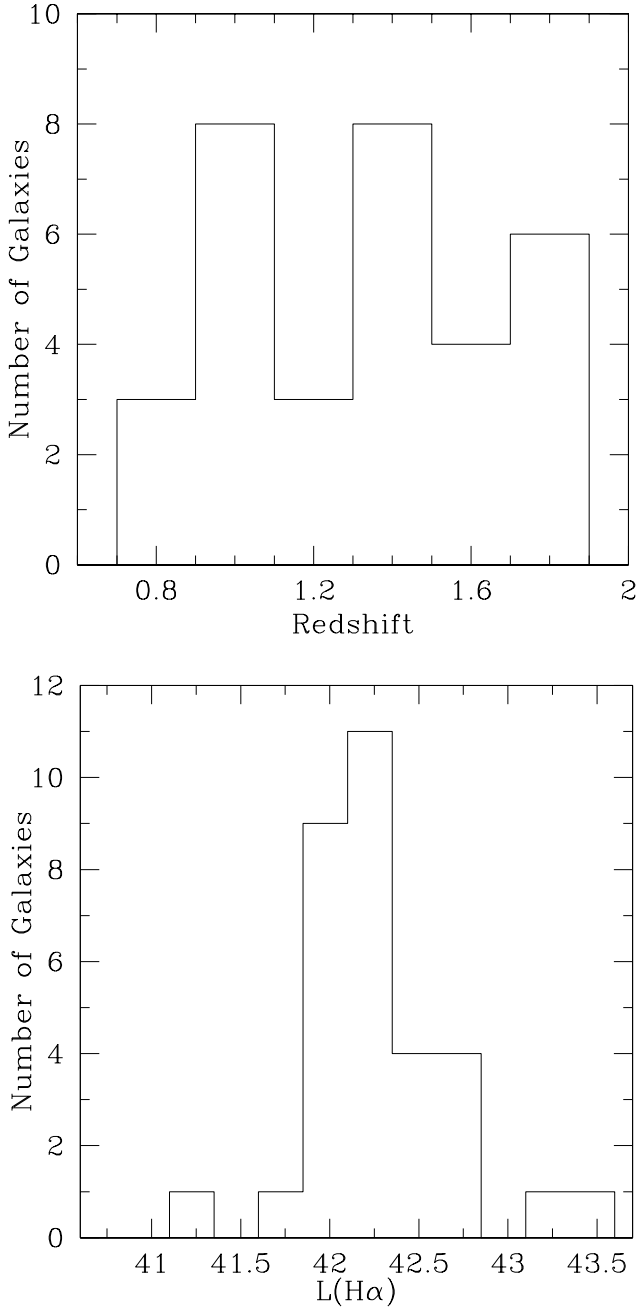

FIG. 6.—Distributions of redshifts and Hα line luminosities of the emission-line galaxies.

We thank the staff of the Space Telescope Science Institute for their efforts in making this parallel program possible. In particular we thank Peg Stanley, Doug van Orsow, and the staff of the PRESTO division. We also thank John Mackenty and members of the STScI NICMOS group for crafting the exposure sequences, and we acknowledge the role of Duccio Macchetto and the Parallel Working Group, led by Jay Frogel, in making the public parallel program a success. This research was supported in part by grants from the Space Telescope Science Institute, GO-7498.01-96A and P423101. H. I. T. and J. P. G. acknowledge funding by the Space Telescope Imaging Spectrograph Instrument Definition Team through the National Optical Astronomy Observatories and by the NASA Goddard Space Flight Center.

REFERENCES

Bechtold, J., Elston, R., Yee, H. K. C., Ellingson, E., & Cutri, R. 1998, in ASP Conf. Ser. 146, The Young Universe, ed. S. D'Odorico, A. Fontana, & E. Giallongo (San Francisco: ASP), 241
Beckwith, S. V. W., Thompson, D., Mannucci, F., & Djorgovski, S. G. 1998, ApJ, 504, 107
Dey, A., Spinrad, H., Stern, D., Graham, J. R., & Chaffee, F. 1998, ApJ, 498, 93L
Dickinson, M. 1999, in The Hubble Deep Field, ed. M. Livio, M. Fall, & P. Madau (Baltimore: STScI), in press
Ellis, R., Colless, M., Broadhurst, T., Heyl, J., & Glazebrook, K. 1996, MNRAS, 280, 235
Freudling, W., & Pirzkal, N. 1998, in ESO Conf. 55, NICMOS and the VLT: A New Era of High Resolution Near Infrared Imaging and Spectroscopy, ed. W. Freudling & R. Hook (Garching: ESO), 47
Gallego, J., Zamorano, J., Rego, M., & Vitores, A. G. 1997, ApJ, 475, 502
Giavalisco, M., et al. 1999, in preparation
Glazebrook, K., Blake, C., Economou, F., Lilly, S., & Colless, M. 1998, preprint (astro-ph/9808276)

Hammer, F., et al. 1997, ApJ, 481, 49
Heckman, T., Robert, C., Leitherer, C., Garnett, D. R., & van der Rydt, F. 1998, ApJ, 503, 646
Hewett, P., Foltz, C. B., & Chaffee, F. H. 1993, ApJ, 406, L43
Hu, E. M., Cowie, L. L., & McMahon, R. G. 1998, ApJ, 502, L99
Kennicutt, R. C. 1992, ApJ, 388, 310
Kennicutt, R. C., Bothun, G. D., & Schommer, R. A. 1984, AJ, 89, 1279
Le Fevre, O., Hudson, D., Lilly, S. J., Crampton, D., Hammer, E., & Tresse, L. 1996, ApJ, 461, 534
Lilly, S. J., Le Fevre, O., Hammer, F., & Crampton, D. 1996, ApJ, 460, L1
Lin, H., Kirshner, R. P., Shectman, S. A., Landy, S. D., Oemler, A., Tucker, D. L., & Schechter, P. L. 1996, 464, 60
Mannucci, F., Thompson, D. J., Beckwith, S. V. W., & Williger, G. M. 1998, ApJ, 501, 11
Meurer, G. R., Heckman, T. M., Lehnert, M. D., Leitherer, C., & Lowenthal, J. 1997, AJ, 114, 54
Neugebauer, G., Soifer, B. T., Miley, G. K., & Clegg, P. E. 1986, ApJ, 308, 815
Pettini, M., Kellogg, M., Steidel, C. C., Dickinson, M., Adelberger, K. L., & Giavalisco, M. 1998, ApJ, 508, 539
Smail, I., Ivison, R. J., Blain, A. W., & Kneib, J. P. 1998, ApJ, 507, L21
Spinrad, H., Stern, D., Bunker, A., Dey, A., Lanzetta, K., Yahil, A., Pascarelle, S., & Fernández-Soto, A. 1998, AJ, 116, 2617
Steidel, C., Giavalisco, M., Pettini, M., Dickinson, M., & Adelberger, K. 1996, ApJ, 462, L17
Teplitz, H. I., Malkan, M. A., & McLean, I. S. 1999a, ApJ, 514, 33
———. 1999b, AIP Conf. Proc. 470, After the Dark Ages (New York: AIP), 364
Teplitz, H. I., McLean, I. S., & Malkan, M. A. 1999c, ApJ, 520, 469
Thompson, D. J., Mannucci, F., & Beckwith, S. V. W. 1996, AJ, 112, 1794
Thompson, R. I., Rieke, M., Schneider, G., Hines, D. C., & Corbin, M. R. 1998, ApJ, 492, L95
Tresse, L., & Maddox, S. 1998, ApJ, 495, 691
Tresse, L., Rola, C., Hammer, F., Stasinska, G., Le Fevre, O., Lilly, S. J., & Crampton, D. 1996, MNRAS, 281, 847
Weymann, R., Stern, D., Bunker, A., Spinrad, H., Chaffee, F., Thompson, R. I., & Storrie-Lombardi, L. J. 1998, ApJ, 505, L95
van der Werf, P. P., Bremer, M. N., Moorwood, A. F. M., & Rottgering, H. J. A. 1997, in IAU Symp. 186, Galaxy Interactions at High and Low Redshift, ed. D. Sanders (Dordrecht: Kluwer), 197
Yan, L., et al. 1999, ApJ, 519, L47
Yan, L., McCarthy, P. J., Freudling, W., Teplitz, H. I., Malumuth, E. M., Weymann, R. J., & Malkan, M. A. 1999, ApJ, submitted
Yee, H. K. C., Ellingson, E., & Carlberg, R. G. 1996, ApJS, 102, 269